Journal of Materials Chemistry C

PAPER

View Article Online
View Journal | View Issue



Cite this: J. Mater. Chem. C, 2016, 4, 3555

# Functionalized multi-wall carbon nanotubes/$TiO_2$ composites as efficient photoanodes for dye sensitized solar cells

Daniele Benetti,†[a] Kadiatou Therese Dembele,†[a] Jaime Benavides,[b] Haiguang Zhao,[ac] Sylvain Cloutier,[b] Isabella Concina,[cde] Alberto Vomiero*[ae] and Federico Rosei*[afg]

Received 24th February 2016,
Accepted 18th March 2016

DOI: 10.1039/c6tc00800c

www.rsc.org/MaterialsC

We report on the effects of incorporation of different concentrations of carboxyl group (COOH)-functionalized multi-wall carbon nanotubes (F-MWCNTs) into $TiO_2$ active layers for dye-sensitized solar cells (DSSCs). Standard DSSCs with bare $TiO_2$ exhibit a photo-conversion efficiency (PCE) of 6.05% and a short circuit current density ($J_{sc}$) of 13.3 mA $cm^{-2}$. The presence of 2 wt% F-MWCNTs in the photoanodes increases the PCE up to 7.95% and $J_{sc}$ up to 17.5 mA $cm^{-2}$. The photoanodes were characterized using scanning electron microscopy (SEM), Fourier transform infrared (FTIR) spectroscopy and Raman spectroscopy. The electrochemical behaviour of the solar cells was investigated by electrochemical impedance spectroscopy (EIS). We attribute the improved performances to the combined effect of increased dye loading and reduced charge recombination (as clarified by dye loading and EIS measurements), due to the conformal coverage of F-MWCNTs, which allows fast and efficient charge collection in operating solar cells. These results can help in improving the PCE in DSSCs in an elegant and straightforward way, minimizing the need of additional steps (*e.g.* pre- and post-treatment with $TiCl_4$) for photoanode preparation.



## Introduction

Dye sensitized solar cells (DSSCs) have been studied extensively in the last two decades because of their promising photo-conversion efficiency (PCE), simple fabrication process, low production costs and the use of environmentally friendly materials.[1,2] They represent a credible alternative to silicon-based solar cells, particularly for niche markets. In the past few years renewed interest for this kind of devices has emerged, thanks to discoveries in the design of new dyes and electrolytes, boosting the PCE up to 14%.[3–5] The basic configuration of DSSCs consists of three main parts: a transparent conducting oxide (TCO) (such as fluorine-doped tin oxide, FTO) on glass, a mesoporous metal oxide semiconductor (such as $TiO_2$) film sensitized by a monolayer of dye molecules grafted on the oxide surface, and a counter electrode (CE) (usually platinum-coated FTO). The cell is then filled with an electrolyte that serves as a hole transport material (HTM).

The metal oxide semiconductors used as the photoanode are critical for photovoltaic (PV) performance.[6] Variations in the structure and morphology of the metal oxide can greatly affect the PCE since it is directly related to the charge transport and dye loading.[7,8]

Although mesoporous photoanodes offer good performances, largely due to light harvesting of the dye-sensitized nanocrystalline film, there are some drawbacks: while offering an extremely high specific surface for dye loading, mesoporous networks suffer from a high density of grain boundaries, which promote charge recombination in operating devices.[6]

Different strategies have been proposed to increase charge collection, such as the use of various metal oxide semiconductors, particularly one dimensional (1D) nanostructures like nanorods (NRs),[9,10] nanowires (NWs)[11–13] and nanotubes (NTs)[14–17] based electrodes.

Among these various 1D nanostructures, the carbon-based ones are particularly interesting. Since their discovery in 1991,[18]

[a] INRS Centre for Energy, Materials and Telecommunications, 1650 Boul. Lionel Boulet, J3X 1S2 Varennes, QC, Canada. E-mail: rosei@emt.inrs.ca
[b] Département de Génie Électrique, École de technologie supérieure, 1100 rue Notre-Dame Ouest, H3C 1K3 Montréal, QC, Canada
[c] CNR-INO SENSOR Lab, Via Branze, 45, 25123 Brescia, Italy
[d] SENSOR Lab, Department of Information Engineering, University of Brescia, Via Valotti 9, 25133 Brescia, Italy
[e] Division of Materials Science, Department of Engineering Sciences and Mathematics, Luleå University of Technology, 971 87 Luleå, Sweden. E-mail: alberto.vomiero@ltu.se
[f] Institute for Fundamental and Frontier Science, University of Electronic Science and Technology of China, Chengdu 610054, P. R. China
[g] Center for Self-Assembled Chemical Structures, McGill University, 801 Sherbrooke Street West, H3A 2K6 Montréal, Québec, Canada
† These authors contributed equally.

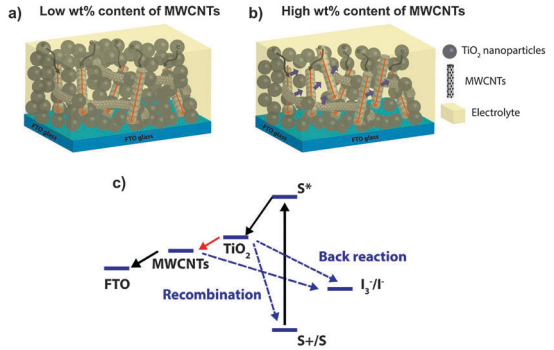


Scheme 1 (a) Schematic illustration of the concept of improved charge collection in a photoanode based on a composite system with CNTs embedded in a $TiO_2$ mesoporous structure. (b) At high CNT concentration, CNT agglomeration enables direct contact between the CNTs and the electrolyte, adding a new recombination pathway (blue arrows). (c) Electronic band diagram of the DSSC functionalized with CNTs.

carbon nanotubes (CNTs) have played a significant role in the development of alternative clean and sustainable energy technologies,[19] due to their extraordinary electronic and mechanical properties.[20] The incorporation of low-dimensional carbon nanostructures such as CNTs[21–23] and graphene sheets[24–26] into semiconductor electrodes was recently proposed to improve the charge collection and PV performance of DSSCs. CNTs were shown to enhance the electron transport inside $TiO_2$ based DSSCs.[27] They are suitable to be used in combination with $TiO_2$, thanks to the good electron band alignment with $TiO_2$ and the FTO conducting glass (see Scheme 1), offering a more efficient pathway for the collection and transport of photogenerated electrons. However, due to their high surface area, CNTs tend to agglomerate in bundles, thereby reducing the solubility in most solvents, which could reduce the ability to be dispersed, when mixed with $TiO_2$.[28] A non-homogenous dispersion of CNTs into the $TiO_2$ paste could negate their beneficial effects. Therefore, the ability to homogeneously disperse CNTs inside the $TiO_2$ matrix as well as the ability to produce a strong interfacial interaction are key challenges in maximizing the contribution of CNTs for their application in DSSCs.[23]

Here, we report a systematic investigation of the role of functionalized multi-wall carbon nanotubes (F-MWCNTs) in a $TiO_2$ photoanode. We used an acid modification to achieve F-MWCNTs, to improve their stability in polar solution and hence increase their homogenous dispersibility in the $TiO_2$ matrix.[29] In addition, the functionalization introduces chemical groups (*e.g.* carboxylic groups) that can increase the interaction with the $TiO_2$ nanoparticles and enables a better coverage of F-MWCNTs with titania.

The presence of carboxylic groups on the CNTs could intensify the interactions with $TiO_2$ increasing their dispersibility into the $TiO_2$ matrix, thereby avoiding the formation of cracks even at high loads (cracks start to appear around 3.5 wt%). In this way, we were able to investigate the effects of F-MWCNTs in a wide concentration range, up to 4 wt%. In previous studies, instead, the concentration range was up to only 0.2–0.3 weight percent (wt%)[21,23,30] due to the lower dispersibility of the CNTs that causes cracks in $TiO_2$ starting from 0.25 wt%.[27]

At an optimal F-MWCNT concentration, this highly reproducible process leads to more than 30% improvement in the PCE of the DSSCs with respect to the bare $TiO_2$ photoanode. This result is quite remarkable since we used a standard dye molecule (N719) and no surface modification treatments of the photoanode and/or addition of blocking layers were performed (such as $TiCl_4$ to boost the open circuit photovoltage ($V_{oc}$)). The role of F-MWCNTs in the charge transfer in operating DSSC devices was investigated by electrochemical impedance spectroscopy (EIS), helping us to identify the physical–chemical mechanism that underpins the increase in PCE.

## Experimental

The $TiO_2$ anatase nanoparticle paste was purchased from DyeSol and the standard MWCNTs (>95% Carbon, Sigma-Aldrich, cat. no. 698849, 10 μm average length) were functionalized following the method described by Osorio *et al.*[29] According to the method described previously,[27] a simple mixing approach was chosen for addition of F-MWCNTs to the $TiO_2$ paste. A precise amount of F-MWCNT solution was mixed by mechanical stirring with a known weight of $TiO_2$ until full incorporation was achieved (this process usually takes 5 min). The F-MWCNT/$TiO_2$ composite and bare $TiO_2$ were tape casted on FTO glass followed by a drying process in ambient atmosphere and room temperature for 15 min and then 6 min at 150 °C. Afterwards, the photoanodes were annealed at 200 °C for 15 min, at 400 °C for 15 min and at 500 °C for 30 min. The prepared photoanodes were further sensitized with the N719 dye (0.5 mM in ethanol, Sigma Aldrich) for 24 h.

Different photoanodes containing various percentages of F-MWCNTs from 1 wt% up to 4 wt% were prepared. The final percentage of F-MWCNTs incorporated in the $TiO_2$ photoanodes was estimated taking into account the photoanode weight before and after annealing. From previous work, the weight loss of the $TiO_2$ paste after annealing is 80% of the original net weight.[27]

The DSSCs were fabricated by using the $I^{3-}/I^-$ redox couple electrolyte (Solaronix, Iodolyte HI-30), platinized FTO glass as the CE (a 5 nm thin film of Pt sputter-deposited on FTO), and a 25 μm thick plastic spacer between the photoanode and the Pt CE.

The structure and morphology of the photoanodes with or without F-MWCNTs were characterized by scanning electron microscopy (SEM, FE-SEM LEO 1525 microscope) and atomic force microscopy (AFM, Veeco Enviroscope). To investigate the presence of F-MWCNTs after annealing, Raman spectroscopy and diffuse reflectance Fourier-transform infrared (DRIFT) analysis were performed. DRIFT was carried out in a Bruker Vertex 70v Spectrometer recording 32 scans at 4 $cm^{-1}$ resolution and displayed in Kubelka–Munk units.[31,32] KBr was used as a background. Samples with the highest nominal amount of F-MWCNTs were chosen for both analyses.

We investigated the effect of F-MWCNTs on the optical absorbance using UV-Visible spectroscopy.

Dye loading was quantitatively evaluated using UV-Vis spectrophotometry after complete removal of the dye from the photoanode.

 

The photoanode was scraped off, weighed and dissolved in a known amount of ethanol (3 mL). After sonication (30 min) and centrifugation (15 min @ 5000 rpm), the $TiO_2$ particles were removed and the absorbance of the solution was measured. Using a fitted calibration curve obtained from solutions of known N719 concentrations the dye loading was then extrapolated using the 500 nm peak. The volume density was calculated by dividing the mass of the photoanode by its volume.

The current–voltage ($I$–$V$) characteristics of the fabricated cells were measured using a Keithley 2400 SourceMeter under simulated sunlight using an ABET2000 solar simulator at AM 1.5G (100 mW $cm^{-2}$) calibrated using a reference silicon cell and mechanical filters. The external quantum efficiency (EQE) spectra were acquired in the dark using an EQE 200 Oriel integrated system. The measurement step was 10 nm and the photocurrent was recorded using a lock-in amplifier.

Electrochemical impedance spectroscopy (EIS) was conducted in the dark using a SOLARTRON 1260 A Impedance/Gain-Phase Analyzer. The AC signal was 10 mV in amplitude, in the frequency range between 100 mHz and 300 kHz. The applied bias during measurements was between 0 and 200 mV above the open-circuit voltage of the solar cell under illumination. All the samples were measured inside a Faraday cage. The obtained spectra were fitted with Z-View software (v3.0, Scribner Associate, Inc.) by applying an appropriate equivalent circuit.

## Result and discussion

The Raman spectra of the MWCNTs before and after the acid treatment are shown in Fig. 1. The D and G bands characteristic of CNTs are clearly observed at 1330 $cm^{-1}$ and 1580 $cm^{-1}$, respectively. They can be attributed to CNT defects (band at 1330 $cm^{-1}$), a disorder-induced mode, and an in-plane $E_{2g}$ zone-center mode.[23] As expected, after functionalization, the ratio between the intensities of these two bands increases due to the formation of surface defects in CNTs as a consequence of the insertion of chemical groups and bond breaking.[29,33]

In Fig. 1c and d a comparison of MWCNT and F-MWCNT dispersion in ethanol at different times is shown. MWCNTs undergo strong precipitation, while no optical difference can be appreciated for F-MWCNTs in solution. The presence of hydroxyl and carboxylic groups keep the MWCNTs stable in solution up to 6 months (not shown here).

In Fig. 2, the AFM images of the MWCNTs are shown. The samples were prepared by spin-coating a diluted solution of a mixture of $TiO_2$ and F-MWCNTs (or MWCNTs) on FTO to obtain a thin film in which the CNTs were visible. In both cases (Fig. 2b and c), the CNTs were conformally covered by $TiO_2$ nanoparticles.

The SEM images of the F-MWCNT/$TiO_2$ composite photoanode films are shown in Fig. 3. Typically, F-MWCNT concentrations up to 2 wt% are not visible by SEM imaging[21] (Fig. 3a and b) due to conformal coverage and the absence of cracks.

From our analyses, the coverage of F-MWCNTs by $TiO_2$ NPs is similar to what has been reported in the literature for

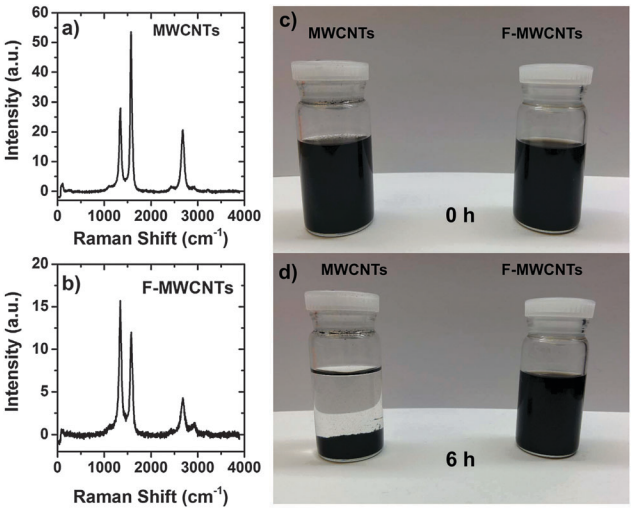


Fig. 1 Raman spectra of the (a) MWCNTs and (b) F-MWCNTs. In (c) and (d) is reported a dispersion of MWCNTs and F-MWCNTs in ethanol solution at 0 h and after 6 h, respectively.

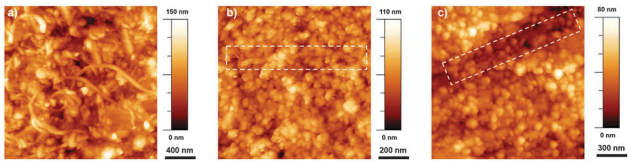

Fig. 2 AFM images of (a) F-MWCNTs on FTO, (b) F-MWCNT/$TiO_2$ and (c) MWCNT/$TiO_2$. The dashed squares highlight the presence of the CNTs.

analogous systems:[27,34] the $TiO_2$ NPs conformally cover the CNTs (and graphene sheets in the case of graphene addition), making them almost invisible by SEM observation. High resolution TEM applied to similar systems was unable to identify any difference in the grafting of $TiO_2$ NPs to the CNT/graphene structure. The main difference induced by the presence of MWCNTs (or graphene) in the composite is the variation of density/porosity (as demonstrated below through AFM) and the formation of deep cracks at high MWCNT concentration. We were able to detect F-MWCNTs only in the 4 wt% sample. A high F-MWCNT load leads to a less compact $TiO_2$ layer and can induce some cracks in the film, as visible in Fig. 3c–f. At this high percentage, it is possible to observe F-MWCNT aggregates conformally covered by $TiO_2$ nanoparticles. Fig. 3c and d show some F-MWCTNs, covered by $TiO_2$ nanoparticles, confirming their presence inside the metal oxide scaffold after high-temperature annealing. To investigate the effects of F-MWCNTs on the absorbance in the visible range, UV-Visible absorption spectroscopy was performed on samples containing various percentages of F-MWCNTs. The results in Fig. 4 suggest a slight increase in absorbance from 0 to 4 wt% F-MWCNTs. The absorbance from F-MWCNTs is in competition with the absorbance from the dye for charge photogeneration, as photons absorbed by F-MWCNTs do not contribute to the photocurrent and are lost, thus affecting the performance of the cell.

However, the slight increase of absorbance even in the sample with a higher F-MWCNT concentration calls for a minor

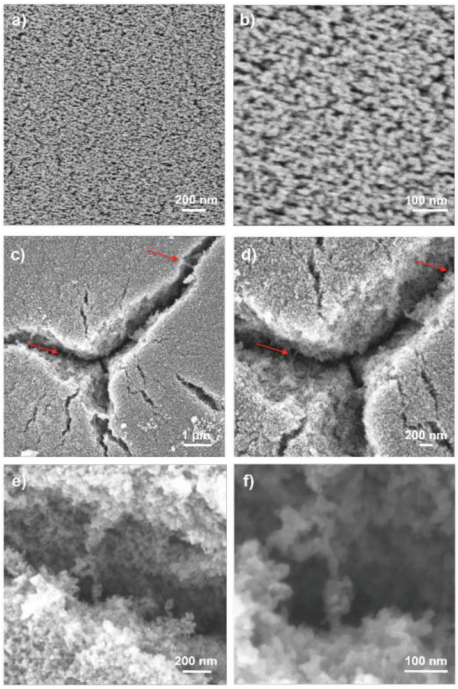


Fig. 3 SEM images at different magnifications of 2 wt% F-MWCNT/$TiO_2$ photoanode (a and b), and 4 wt% F-MWCNT/$TiO_2$ photoanode (c–f). Red arrows indicate the F-MWCNTs, partially covered by $TiO_2$ NPs.

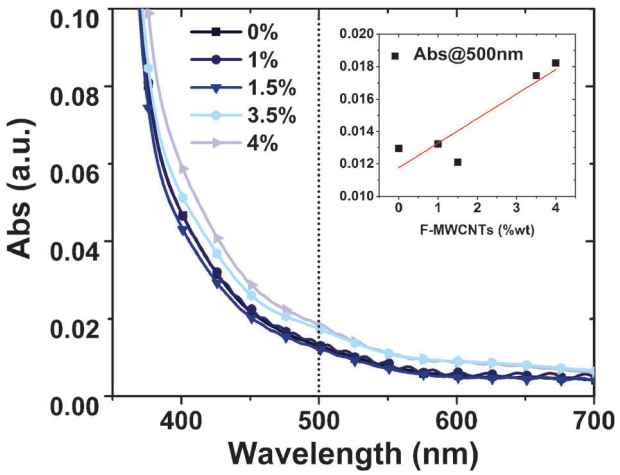


Fig. 4 Absorbance spectra of various samples containing different percentages of F-MWCNTs. The increase in absorbance is highlighted in the inset that reports the change in absorbance at 500 nm for different F-MWCNT concentrations.

contribution of this effect in impairing PCE. Further confirmation of the presence of F-MWCNTs inside the titania matrix after the annealing process was obtained from DRIFT and Raman spectroscopies.

The Raman spectrum of a typical $TiO_2$/F-MWCNT nanocomposite is shown in Fig. 5a. Similar results are obtained, independent of the F-MWCNT concentration. The three intense bands at 394.7, 514.5 and 637.2 $cm^{-1}$ are ascribed to the the $B_{1g}$, $A_{1g}$ + $B_{2g}$ and $E_g$ modes of anatase $TiO_2$, respectively.[35]

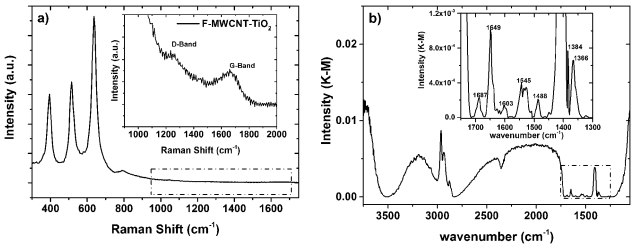


Fig. 5 (a) Raman spectrum and (b) FTIR spectrum of a typical MWCNT/$TiO_2$ photoanode. The insets are magnified view of the dashed regions.

The D (disordered carbon induced) and G (graphite carbon related) bands are represented respectively at 1200 $cm^{-1}$ and 1650 $cm^{-1}$, indicating the co-existence of $TiO_2$ and F-MWCNTs in the nanocomposite. These bands can be attributed to CNT defects and a disorder-induced mode as well as an in-plane $E_{2g}$ zone-center mode.[23]

The DRIFT spectrum (4000–400 $cm^{-1}$) of a typical photoanode containing F-MWCNTs is shown in Fig. 5b. Similar results are obtained, independent of the F-MWCNT concentration. The stretching modes of C–H bonds are clearly visible in the region 3000–2800 $cm^{-1}$, where asymmetrical and symmetrical stretching vibrations of $–CH_2$ and $–CH_3$ groups can be observed. The region from 3500 to 3000 $cm^{-1}$ is dominated by the stretching vibration of –OH groups: the associated band is relatively sharp and the typical, very broad shoulder usually associated with the stretching vibration of hydroxyls in carboxylic acids is absent. This suggests that the –COOH groups generated in the functionalization process of MWCNTs are no longer present, while the carbon materials are inserted in the $TiO_2$ scaffold. This hypothesis is also confirmed by the analysis of the fingerprint region (inset in Fig. 5b), where, together with the stretching mode of C=O (1649 $cm^{-1}$), symmetrical and asymmetrical stretching vibrations of O–C–O groups are recorded (1488 $cm^{-1}$ and 1405 $cm^{-1}$, respectively).

To further analyze the effect of the addition of F-MWCNTs, we investigated the surface morphology of the samples by AFM. A variation in film roughness is clearly visible from the AFM images reported in Fig. 6, in which three samples at different F-MWCNT concentrations are analyzed: 0, 2 and 4 wt%, respectively. A different dimension of the pores visible at the surface of the $TiO_2$ film is apparent, and it is observed to increase with the increasing of the percentage of F-MWCNTs.

The previous work reported that the introduction of F-MWCNTs into a $TiO_2$ matrix generally induces better separation of $TiO_2$ particles, consequently resulting in a structure with a higher porosity and surface area.[21,28,36]

The addition of F-MWCNTs up to a medium load (2 wt%) enlarges the network of $TiO_2$, thus leading to larger surface pores. It is likely that increased porosity reflects not only at the surface of the film, but also in its bulk, leading to a larger surface area, as also confirmed from the dye loading quantification reported below. Further increase of the amount of CNTs leads to the formation of agglomerates resulting in irregular and large pore sizes that can affect the roughness of the

 

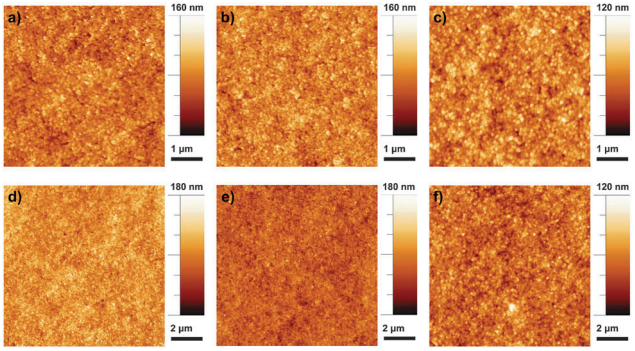


Fig. 6 AFM images of sample with different concentrations of F-MWCNTs: (a, b and c) 0 wt%, 2 wt%, 4 wt% on 5 μm × 5 μm; (d, e and f) 0 wt%, 2 wt%, 4 wt% on 10 μm × 10 μm.

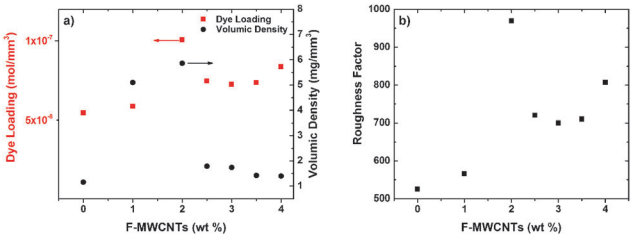


Fig. 7 (a) Dye loading (left) and volume density (right) of samples at different loads of F-MWCNTs. The optimum value of F-MWCNTs (2 wt%) corresponds to the maximum of dye loading and volume density. (b) Roughness factor calculated for different loads of F-MWCNTs.

photoanode and reduce the specific surface area (decreasing consequently the dye loading).

A further confirmation of this phenomenon comes from the analysis of dye loading (Fig. 7a). Both dye loading and volume density increase with the increase of the F-MWCNT amount (up to 2 wt%) and then start to decrease again upon further F-MWCNT addition. The data indicate that at an optimum F-MWCNT loading (2 wt%) an electrode with the maximum porosity and specific surface area is formed, which maximize the dye loading and optical density of the photoanode. The quantitative parameter to estimate the available surface for a certain photoanode is the so-called roughness factor, which is defined as the total available surface per sample area. It can be calculated by taking into account the measured dye loading and film thickness, under the hypothesis of monolayer dye absorption on the $TiO_2$ surface. Fig. 7b displays the values of the roughness factor as a function of F-MWCNT concentration for samples with the same thickness (mandatory for a fair comparison of different samples). A value of 1.6 $nm^2$ per dye molecule was used to estimate the roughness factor.[37] This estimation indicates that the photoanode surface roughness increases with the incorporation of F-MWCNTs up to 2 wt%, while it decreases at higher loads.

We investigated the effect of different F-MWCNT loadings on the functional properties of DSSCs. The *J*–*V* curves of selected cells under AM 1.5G simulated sunlight and the external quantum efficiency (EQE) are reported in Fig. 8a and b. Table 1 reports

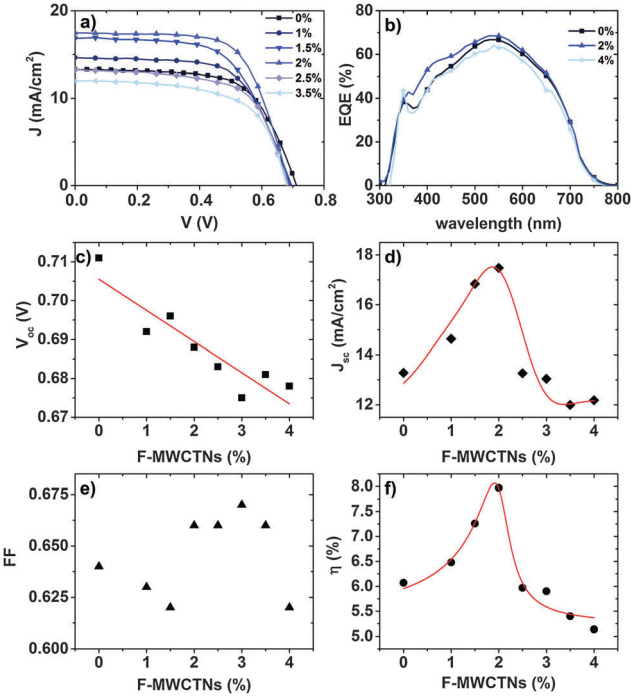


Fig. 8 (a) *J*–*V* curves of DSSCSs at six different percentages of F-MWCNTs under simulated sunlight (AM 1.5G, 100 mW $cm^{-2}$). (b) EQE of the most representative samples. (c–f) Variation of functional parameters ($V_{oc}$, $J_{sc}$, FF, and PCE) as a function of the F-MWCNT loading. Red lines are a guide for the eye.

Table 1 Functional characteristics of the DSSCs

| [F-MWCNTs] (wt%) | $V_{oc}$ (V) | $J_{sc}$ (mA $cm^{-2}$) | FF | PCE (%) |
|---|---|---|---|---|
| 0 | 0.710 ± 0.01 | 12.9 ± 0.4 | 0.65 ± 0.02 | 6.05 ± 0.05 |
| 1 | 0.690 ± 0.01 | 14.80 ± 0.55 | 0.63 ± 0.01 | 6.55 ± 0.05 |
| 1.5 | 0.695 ± 0.01 | 16.85 ± 0.01 | 0.62 ± 0.01 | 7.15 ± 0.15 |
| 2 | 0.690 ± 0.01 | 17.50 ± 0.05 | 0.66 ± 0.01 | 7.85 ± 0.10 |
| 2.5 | 0.685 ± 0.005 | 13.2 ± 0.1 | 0.66 ± 0.01 | 5.95 ± 0.05 |
| 3 | 0.670 ± 0.005 | 12.8 ± 0.4 | 0.66 ± 0.01 | 5.70 ± 0.20 |
| 3.5 | 0.685 ± 0.005 | 12.00 ± 0.05 | 0.67 ± 0.01 | 5.50 ± 0.20 |
| 4 | 0.675 ± 0.005 | 12.15 ± 0.05 | 0.64 ± 0.05 | 5.30 ± 0.20 |

the PV parameters ($V_{oc}$, short circuit current density ($J_{sc}$), fill factor (FF), and PCE). The trend of PV parameters as a function of F-MWCNT loading is reported in Fig. 8c–f.

Compared with bare $TiO_2$, the F-MWCNT/$TiO_2$-based DSSC with concentrations up to 2 wt% showed a higher PCE. At an optimum concentration of 2 wt%, we obtained the maximum increase resulting in a PCE as high as 7.95%, with an enhancement of around 30% with respect to pure $TiO_2$ (6.05%).

The presence of F-MWCNTs in the concentration range up to 2 wt% significantly boosts $J_{sc}$ compared to pure $TiO_2$ photoanodes, while the other cell parameters ($V_{oc}$, FF) do not play a major role in altering PCE.

The $J_{sc}$ value reaches its maximum in the 2 wt% sample and then suddenly decreases at higher F-MWCNT concentrations: 2.5 wt% of F-MWCNTs results in a $J_{sc}$ almost equal to the pure $TiO_2$ sample. The EQE on selected samples (0 wt%, 2 wt% and 4 wt%)

confirms the trend with higher values for the samples at 2 wt%. $V_{oc}$ is slightly but systematically affected by the presence of F-MWCNTs. As pointed out by several recent studies,[25–27,38] the addition of carbonaceous materials results in a decrease of $V_{oc}$, most probably due to the downshift of the conduction band in the composite system, compared to pure $TiO_2$,[25] as the $V_{oc}$ is determined by the difference between the redox potential of the electrolyte and the Fermi level of $TiO_2$.[39,40] The larger the F-MWCNT concentration, the larger the expected $V_{oc}$ decrease, as found in our cells. The decrease is of the order of a few tens of mV (32 mV between the pure $TiO_2$ and the 4 wt% sample), which does not significantly affect the increase in PCE which is prompted by the current density increase. This result is in contrast to that observed by Kamat in 2008.[41] In that case, however, the CNT concentration was much larger, as the photoanode was essentially composed of CNTs covered by $TiO_2$ nanoparticles. Therefore, the $V_{oc}$ decrease was much more pronounced and led to a strong decrease of PCE. Another possible concurring reason for this behaviour at high MWCNT concentrations could be the partial coverage of the surface of the F-MWCNTs by the $TiO_2$ nanoparticles, which leave CNTs in direct contact with the electrolyte.[24,42] This creates a preferential path for charge recombination, which results in charge loss and a decrease in $V_{oc}$.

We applied EIS to gain insight into the changes induced by the presence of F-MWCNTs on the physical and chemical processes which take place in the operating device. In particular, we focused on the recombination resistance $R_{rec}$ and the chemical capacitance $C_{\mu}$. We could not observe the transport resistance due to the large conductivity of the samples.[43,44]

Fig. 9a compares the Nyquist plots of three different cells (bare $TiO_2$, 2 wt% and 4 wt%) at a bias voltage equal to $V_{oc}$. Three semicircles are clearly observable in the measured frequency range from 100 mHz to 300 kHz and are located in the high, intermediate and low frequency regimes, from left to right, respectively. The arc at high frequencies is assigned to the impedance of the electron transfer at the Pt CE, the one at intermediate frequencies corresponds to the recombination at the $TiO_2$ surface, and the last one at low frequencies represents the ionic diffusion process inside the electrolyte.[43,45,46] The most remarkable feature is that the 2 wt% cell leads to the smallest arcs at midfrequencies, related to the recombination at the $TiO_2$ surface. The medium arc takes into account the recombination resistance of the mesoporous layer: for the cell exploiting 2 wt% F-MWCNTs this feature is much smaller compared to the others. This behaviour indicates that the presence of an optimum amount of F-MWCNTs promotes efficient electron transport, thereby increasing the overall conductivity of the $TiO_2$ matrix.

The peak frequency of the central arc ($\omega_{max}$) in a Nyquist plot gives a simple relationship with the reaction rate constant for recombination.[46] A lower value indicates a lower recombination rate. By extrapolating the $\omega_{max}$ value of the central arc for the three cells, we observe that the smallest one corresponds again to the 2 wt% cell, while the others exhibit values that are 3–4 times higher: 15 Hz (2 wt%) *versus* 60 Hz (4 wt%) and 75 Hz (0 wt%). This means that the recombination rate constant for the cell at 2 wt% is smaller than the other cell. The slower recombination

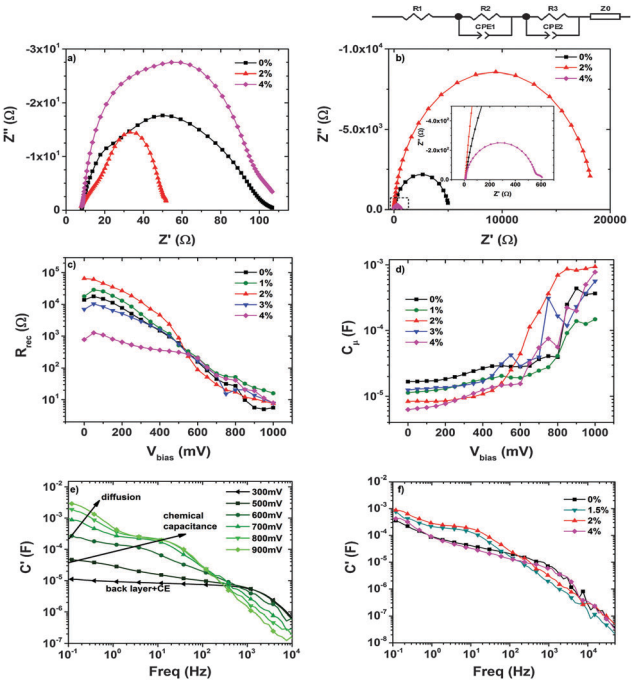


Fig. 9 EIS analysis of DSSCs at different F-MWCNT concentrations. (a) Nyquist plot in the dark at a bias equal to $V_{oc}$; (b) Nyquist plot in the dark at a low bias ($V_{bias}$ = 250 mV) and an equivalent circuit used for fitting the data. The inset is a zoomed-in Nyquist plot of the sample at 4 wt%; (c) recombination resistance and (d) chemical capacitance from EIS measurements in the dark; (e) real part of the capacitance at several applied potentials for the cell with 2 wt% of F-MWCNTs; (f) real part of the capacitance at $V_{bias}$ = $V_{oc}$ for four different concentrations of F-MWCNTs: 0 wt%, 1.5 wt%, 2 wt%, 4 wt%.

rate indicates a larger recombination resistance within the photoanode, resulting in a much slower back-reaction, confirming the beneficial effect of the addition of F-MWCNTs.

A further confirmation of this behaviour is visible in Fig. 9b and c, which reports the $R_{rec}$ of five samples at different F-MWCNT concentrations. Fig. 9b displays the Nyquist plots of three cells at a low voltage bias (250 mV): only a high resistance arc due to the charge recombination and capacitance of the back layer can be appreciated, while the counter electrode contribution is hidden. The increase in recombination resistance in this range is attributed to the reduction of the back reaction between the FTO, the $TiO_2$/F-MWCNT composite and the electrolyte.[44] In Fig. 9c in the region at low potentials (up to 550 mV), where the main contribution comes from the charge transfer from the uncovered FTO substrate at the bottom of the porous film (also called back layer),[47] the resistance follows the same trend as the efficiency: $R_{rec}$ increases from 0% to 2 wt%, while it decreases again at higher F-MWCNT concentrations. Increasing further the amount of F-MWCNTs leads to a decrease of $R_{rec}$ associated with the back reaction. This kind of behaviour can be due to local agglomeration of F-MWCNTs that can create traps and surface defects.

In addition, at high F-MWCNT concentrations, when agglomerates are formed, a direct contact between F-MWCNTs and the electrolyte can occur, which boosts electron loss directly from F-MWCNTs to the electrolyte, further reducing $R_{rec}$.

 

A confirmation of the presence of surface defects can be seen in Fig. 9d that reports the chemical capacitance as a function of the applied bias. The samples with high F-MWCNT concentrations (3 wt% and 4 wt%) exhibit a peak at around 750 mV. This peak is assigned to sub-bandgap-localized states due to defects in the surface, causing a decrease in the efficiency of the cell.[48,49]

Fig. 9e shows the real part of the capacitance *versus* frequency in the 2 wt% cell for several values of the applied biases. The different contributions to the overall capacitance are clearly observable. At a low bias the low frequency limit of the capacitance is due to the contribution of the back layer and the counter electrode. When the bias is increased, the contribution of the chemical capacitance becomes dominant and the contribution from the diffusion in the electrolyte appears at a higher bias. The dominant contribution of the chemical capacitance to the overall capacitance is clearly visible for the cell with 1.5 wt% and 2 wt% of F-MWCNTs as shown in Fig. 9f, while for lower/higher concentrations it is not as prevalent as for the others.

An optimum concentration of F-MWCNTs (2 wt%) exists that maximizes PCE. At higher F-MWCNT loads, nanotube agglomeration tends to be prevalent, compared to the phenomenon of increasing surface area, resulting in a net decrease in PCE. In fact, as highlighted by AFM and dye loading measurements, the presence of conglomerates leads to the formation of large pore sizes above 2 wt% of F-MWCNTs that can reduce the specific surface area. This pore enlargement can bring the F-MWCNT agglomerates in direct contact with the electrolyte, thereby increasing the recombination of the photo-generated electrons (as shown by the EIS analysis), which causes a reduction in the overall efficiency of the cell.

## Conclusions

We demonstrated a fast and highly reproducible methodology to fabricate high performance DSSCs by simple addition of F-MWCNTs into a commercial $TiO_2$ paste. Our results show that incorporating F-MWCNTs into a $TiO_2$ working electrode during the synthesis efficiently improves the physical/chemical properties of the cell, achieving a PCE of 7.95%, which represents more than a 30% increase compared to that in the bare $TiO_2$ sample. The main role of F-MWCNTs is to boost electron injection from the photoanode to the front contact, thereby significantly increasing the collection of photogenerated charges and reducing charge recombination. The enhanced efficiency is also due to the improvement in dye uptake: the presence of F-MWCNTs influences the morphology of the titania matrix, increasing the surface area available at optimal loading values. An excess of F-MWCNTs reduces the open circuit photovoltage, thereby increasing dramatically the charge recombination through direct charge transfer from the photoanode to the electrolyte as shown by EIS analysis. To optimize the amount of F-MWCNTs incorporated into the $TiO_2$ matrix, we used an easy procedure for achieving high dispersibility of CNTs in $TiO_2$. Finally, the proposed methodology is very fast and avoids any surface treatments, which are typically used to boost PCE in standard fabrication procedures of DSSCs.

## Acknowledgements

A. V. is thankful to the European Union for partial salary support under contract No. 299490, MC-IOF and under contract No. 295216, IRSES-WIROX. A. V. is grateful to the Kempe Foundation and LTU Labfonden program for funding for equipment. F. R. is grateful to NSERC for funding and partial salary support through a EWR Steacie Memorial Fellowship and the Alexander von Humboldt Foundation for a FW Bessel Award. F. R. acknowledges the FQRNT for funding through team projects, and funding from MDEIE for an international collaboration grant in collaboration with the European Network WIROX. H. Z. acknowledges NSERC for a postdoctoral fellowship. IC thanks VINNOVA for partial salary support under the Project "Light Energy" (LiEn).

## Notes and references

1 B. O'Regan and M. Grätzel, *Nature*, 1991, **353**, 737–740.
2 M. Grätzel, *J. Photochem. Photobiol., C*, 2003, **4**, 9.
3 B. E. Hardin, H. J. Snaith and M. D. McGehee, *Nat. Photonics*, 2012, **6**, 162–169.
4 A. Yella, H. W. Lee, H. N. Tsao, C. Y. Yi, A. K. Chandiran, M. K. Nazeeruddin, E. W. G. Diau, C. Y. Yeh, S. M. Zakeeruddin and M. Gratzel, *Science*, 2011, **334**, 629–634.
5 S. Mathew, A. Yella, P. Gao, R. Humphry-Baker, B. F. Curchod, N. Ashari-Astani, I. Tavernelli, U. Rothlisberger, M. K. Nazeeruddin and M. Gratzel, *Nat. Chem.*, 2014, **6**, 242–247.
6 M. Gratzel, *Nature*, 2001, **414**, 338–344.
7 E. J. Crossland, N. Noel, V. Sivaram, T. Leijtens, J. A. Alexander-Webber and H. J. Snaith, *Nature*, 2013, **495**, 215–219.
8 Z. Dong, H. Ren, C. M. Hessel, J. Wang, R. Yu, Q. Jin, M. Yang, Z. Hu, Y. Chen, Z. Tang, H. Zhao and D. Wang, *Adv. Mater.*, 2014, **26**, 905–909.
9 B. Liu and E. S. Aydil, *J. Am. Chem. Soc.*, 2009, **131**, 3985–3990.
10 S. H. Kang, S. H. Choi, M. S. Kang, J. Y. Kim, H. S. Kim, T. Hyeon and Y. E. Sung, *Adv. Mater.*, 2008, **20**, 54–58.
11 J. B. Baxter and E. S. Aydil, *Appl. Phys. Lett.*, 2005, **86**, 053114.
12 S. Gubbala, V. Chakrapani, V. Kumar and M. K. Sunkara, *Adv. Funct. Mater.*, 2008, **18**, 2411–2418.
13 X. Feng, K. Shankar, O. K. Varghese, M. Paulose, T. J. Latempa and C. A. Grimes, *Nano Lett.*, 2008, **8**, 3781–3786.
14 A. Vomiero, V. Galstyan, A. Braga, I. Concina, M. Brisotto, E. Bontempi and G. Sberveglieri, *Energy Environ. Sci.*, 2011, **4**, 3408–3413.
15 V. Galstyan, A. Vomiero, I. Concina, A. Braga, M. Brisotto, E. Bontempi, G. Faglia and G. Sberveglieri, *Small*, 2011, **7**, 2437–2442.
16 O. K. Varghese, M. Paulose and C. A. Grimes, *Nat. Nanotechnol.*, 2009, **4**, 592–597.
17 G. K. Mor, K. Shankar, M. Paulose, O. K. Varghese and C. A. Grimes, *Nano Lett.*, 2006, **6**, 215–218.
18 S. Iijima, *Nature*, 1991, **354**, 56–58.
19 H. Zhu, J. Wei, K. Wang and D. Wu, *Sol. Energy Mater. Sol. Cells*, 2009, **93**, 1461–1470.
20 J. Wilder, L. Venema and A. Rinzler, *Nature*, 1998, **584**, 1996–1999.

21 C. Y. Yen, Y. F. Lin, S. H. Liao, C. C. Weng, C. C. Huang, Y. H. Hsiao, C. C. M. Ma, M. C. Chang, H. Shao, M. C. Tsai, C. K. Hsieh, C. H. Tsai and F. B. Weng, *Nanotechnology*, 2008, **19**, 375305.
22 T. Sawatsuk, A. Chindaduang, C. Sae-Kung, S. Pratontep and G. Tumcharern, *Diamond Relat. Mater.*, 2009, **18**, 524–527.
23 Y.-F. Chan, C.-C. Wang, B.-H. Chen and C.-Y. Chen, *Prog. Photovolt. Res. Appl.*, 2013, **21**, 47–57.
24 J. Durantini, P. P. Boix, M. Gervaldo, G. M. Morales, L. Otero, J. Bisquert and E. M. Barea, *J. Electroanal. Chem.*, 2012, **683**, 43–46.
25 K. T. Dembele, G. S. Selopal, R. Milan, C. Trudeau, D. Benetti, A. Soudi, M. M. Natile, G. Sberveglieri, S. Cloutier, I. Concina, F. Rosei and A. Vomiero, *J. Mater. Chem. A*, 2015, **3**, 2580–2588.
26 N. Yang, J. Zhai, D. Wang, Y. Chen and L. Jiang, *ACS Nano*, 2010, **4**, 887–894.
27 K. T. Dembele, G. S. Selopal, C. Soldano, R. Nechache, J. C. Rimada, I. Concina, G. Sberveglieri, F. Rosei and A. Vomiero, *J. Phys. Chem. C*, 2013, **117**, 14510–14517.
28 T. C. A. Jitianu, R. Benoit, S. Delpeux, F. Beguin and S. Bonnamy, *Carbon*, 2004, **42**, 5.
29 I. C. L. S. A. G. Osorio, V. L. Bueno and C. P. Bergmann, *Appl. Surf. Sci.*, 2008, **255**, 5.
30 L. Yang and W. W. Leung, *Adv. Mater.*, 2013, **25**, 1792–1795.
31 F. M. P. Kubelka, *Z. Tech. Phys.*, 1931, **12**, 593–601.
32 G. Kortüm, *Reflectance Spectroscopy*, Springer, New York, 1969.
33 E. Flahaut, C. Laurent and A. Peigney, *Carbon*, 2005, **43**, 375–383.
34 J. Wang, Y. Lin, M. Pinault, A. Filoramo, M. Fabert, B. Ratier, J. Bouclé and N. Herlin-Boime, *ACS Appl. Mater. Interfaces*, 2015, **7**, 51–56.
35 S. P. S. Porto, P. A. Fleury and T. C. Damen, *Phys. Rev.*, 1967, **154**, 522–526.
36 C. Y. Yen, Y. F. Lin, C. H. Hung, Y. H. Tseng, C. C. Ma, M. C. Chang and H. Shao, *Nanotechnology*, 2008, **19**, 045604.
37 M. Grätzel, *Pure Appl. Chem.*, 2001, **73**, 459–467.
38 K. T. Dembele, R. Nechache, L. Nikolova, A. Vomiero, C. Santato, S. Licoccia and F. Rosei, *J. Power Sources*, 2013, **233**, 93–97.
39 S. R. Raga, E. M. Barea and F. Fabregat-Santiago, *J. Phys. Chem. Lett.*, 2012, **3**, 1629–1634.
40 Y.-B. Tang, C.-S. Lee, J. Xu, Z.-T. Liu, Z.-H. Chen, Z. He, Y.-L. Cao, G. Yuan, H. Song, L. Chen, L. Luo, H.-M. Cheng, W.-J. Zhang, I. Bello and S.-T. Lee, *ACS Nano*, 2010, **4**, 3482–3488.
41 P. Brown, K. Takechi and P. Kamat, *J. Phys. Chem. C*, 2008, **112**, 4776–4782.
42 M.-Y. Yen, M.-C. Hsiao, S.-H. Liao, P.-I. Liu, H.-M. Tsai, C.-C. M. Ma, N.-W. Pu and M.-D. Ger, *Carbon*, 2011, **49**, 10.
43 F. Fabregat-Santiago, *J. Phys. Chem. C*, 2007, **2**, 6550–6560.
44 J. Bisquert, I. Mora-Sero and F. Fabregat-Santiago, *ChemElectroChem*, 2014, **1**, 289–296.
45 F. Fabregat-Santiago, J. Bisquert, G. Garcia-Belmonte, G. Boschloo and A. Hagfeldt, *Sol. Energy Mater. Sol. Cells*, 2005, **87**, 117–131.
46 M. Adachi, M. Sakamoto, J. Jiu, Y. Ogata and S. Isoda, *J. Phys. Chem. B*, 2006, **110**, 13872–13880.
47 L. M. Peter, N. W. Duffy, R. L. Wang and K. G. U. Wijayantha, *J. Electroanal. Chem.*, 2002, **524–525**, 127–136.
48 H. Wang, J. He and G. Boschloo, *J. Phys. Chem. B*, 2001, 2529–2533.
49 I. Mora-Sero and J. Bisquert, *Nano Lett.*, 2003, **3**, 945–949.

 